



Topology optimization of structures in transient impacts with Coulomb friction

Kristiansen, Hansotto; Poullos, Konstantinos; Aage, Niels

Published in:
International Journal for Numerical Methods in Engineering

Link to article, DOI:
[10.1002/nme.6756](https://doi.org/10.1002/nme.6756)

Publication date:
2021

Document Version
Peer reviewed version

[Link back to DTU Orbit](#)

Citation (APA):
Kristiansen, H., Poullos, K., & Aage, N. (2021). Topology optimization of structures in transient impacts with Coulomb friction. *International Journal for Numerical Methods in Engineering*, 122, 5053-5075.
<https://doi.org/10.1002/nme.6756>

General rights

Copyright and moral rights for the publications made accessible in the public portal are retained by the authors and/or other copyright owners and it is a condition of accessing publications that users recognise and abide by the legal requirements associated with these rights.

- Users may download and print one copy of any publication from the public portal for the purpose of private study or research.
- You may not further distribute the material or use it for any profit-making activity or commercial gain
- You may freely distribute the URL identifying the publication in the public portal

If you believe that this document breaches copyright please contact us providing details, and we will remove access to the work immediately and investigate your claim.

Topology optimization of structures in transient impacts with Coulomb friction

Hansotto Kristiansen*¹ | Konstantinos Poullos¹ | Niels Aage^{1,2}

¹Department of Mechanical Engineering, Solid Mechanics, Technical University of Denmark, Kongens Lyngby DK-2800, Lyngby, Denmark

²Department of Mechanical Engineering, Solid Mechanics, Centre for Acoustic-Mechanical Micro Systems, Technical University of Denmark, Kongens Lyngby DK-2800, Lyngby, Denmark.

Correspondence

Hansotto Kristiansen, Department of Mechanical Engineering, Solid Mechanics, Technical University of Denmark, Nils Koppels Allé, Building 404, 2800 Kongens Lyngby DK-2800, Lyngby, Denmark. Email: Hakris@mek.dtu.dk

Present Address

Hansotto Kristiansen, Department of Mechanical Engineering, Solid Mechanics, Technical University of Denmark, Nils Koppels Allé, Building 404, 2800 Kongens Lyngby DK-2800, Lyngby, Denmark.

Summary

This paper demonstrates gradient driven density based topology optimization of transient impact problems with friction. The sensitivities are obtained using the semi-discrete adjoint approach in which the temporal components are obtained by the "differentiate then discretize" whereas the spatial part is determined discretely. In this work, the sensitivity analysis method is extended to a mixed formulation involving both displacements, velocities, accelerations and contact forces. The proposed formulation allows to account for frictional impacts during the structural optimization process. A first simple example demonstrates the effects of including frictional impacts into the transient design problem. As a second example, a drop test is considered and a casing for protecting a falling object during a frictional impact, is designed. Solid-void designs are obtained by application of the robust design formulation combined with a parameter continuation scheme.

KEYWORDS:

Topology optimization, Frictional contact, Transient impact, Crashworthiness

1 | INTRODUCTION

Robustness is a much appreciated quality of engineering products. Robust designs are typically favored, not only from a production perspective but also from an operational perspective. From a manufacturing perspective, it is desirable if parts are designed in such a way, that they do not risk malfunctioning due to variances in the manufacturing process. From an operational perspective, robust designs do not fail or malfunction when the operating conditions change. For fixed machinery components this is usually not a big issue, as the loading is typically very stable and well-known. But designing other products, such as handheld devices, is much more demanding as handheld devices are exposed to a wide variety of operational conditions.

It is exactly the latter of the above applications of robustness that motivates this work. The goal is to demonstrate how to account for the possibility of frictional impacts during structural design optimization. Such design problems arise e.g when one wants to guarantee the integrity of a payload during an impact from a drop. This could be the integrity of the glass on a smartphone, the integrity of the insulin cartridge in insulin pens or the body of a moon lander. The numerical examples of the present work do not cover uncertainties on the loading or material properties in a statistical sense. Nevertheless, the deterministic impact scenarios employed, can be seen as extraordinary load cases that the obtained structures are optimized against.

Since Bendsøe and Kikuchi laid the foundation of modern topology optimization with their seminal papers^{1,2}, the method has developed, branched and matured ever since. Nowadays, the density based approach^{3,4,5} still remains as one of the most popular

⁰Abbreviations: ANA, anti-nuclear antibodies; APC, antigen-presenting cells; IRF, interferon regulatory factor

This article has been accepted for publication and undergone full peer review but has not been through the copyediting, typesetting, pagination and proofreading process which may lead to differences between this version and the Version of Record. Please cite this article as doi: 10.1002/nme.6756

methods, however, homogenization methods^{1,6,7}, as a subclass of density based methods, but also level-set methods^{8,9,10,11}, have established well-deserved popularity. For a thorough review of the field of topology optimization see the review paper by Sigmund and Maute¹², from 2013.

All topology optimization methods have, throughout the years, helped engineers optimize and enhance the structural performance of parts and structures. In many engineering situations it is possible to reduce the modeling complexity of a given design problem by neglecting inertia effects. This is often possible e.g for fluid flows in steady-state, static structures like bridges and support structures among many other examples. Reducing the problem at hand to a static problem may be desirable as it alleviates some of the numerical complexity and reduces computational time significantly, but it also leaves the designer blind to dynamic effects such as resonances that can be of critical interest in real-world structures. As the finite element analysis still constitutes the heaviest computational task of any density based topology optimization framework, most of the available literature is based on static assumptions, but of course, topology optimization in a transient setting is possible.

Sensitivity analysis, which is the core of gradient-based topology optimization, has been known for transient problems for a long time^{13,14}, but it was not until recently that transient topology optimization problems became more common^{15,16,17}. With the possibility of transient topology optimization, an intriguing possibility is to design vehicles that will absorb the kinetic energy in a crash by optimizing the material layout in front of the cabin and around the engine - so-called crashworthiness optimization. The literature is full of attempts to perform crashworthiness optimization, of which the majority deals with size optimization of pre-existing parts such as the bumper. An example of size optimization is found in¹⁸, where metamodeling is used to construct a time based objective function of the internal energy in the structure. Because of the very elaborate finite element model of a full Chevrolet S10 pickup truck, limited insight is to be gained from the results, except that the optimized result stores internal energy faster during the impact.

More insight is obtained from the work presented in¹⁹, where ground structures are size optimized to match the desired deceleration at specific points in time, using the relative error at each of these time steps as an objective value and then solving the optimization problem as a min-max problem. In this work, the contact is not modeled, as the structure is fixed and simply subjected to an initial velocity at selected points on the boundary of the design domain. In¹⁹, gradients are evaluated using direct analytical differentiation and structures to decelerate trains, engine mounts and ejection seats, are found. In 2005, Forsberg and Nilsson²⁰ optimized structures for energy absorption, by maximizing the minimum internal energy density of a structure. The impact analysis was performed using LS-DYNA. The design variables were chosen as the thickness of each element, which resembles classic topology optimization. In 2016, Nakshatrala and Tortorelli²¹ designed nonlinear elastodynamic structures with tailored energy propagation subject to impact loading. For a thorough literature review of the field of crashworthiness optimization please confer to the topical review from 2017 by Fang et al²².

Regarding modeling of contact in topology optimization, it should be noted that a considerable amount of attention has been given to problems concerning static contact problems. The majority of these consider compliance minimization under quasistatic loading^{23,24,25,26,27,28,29}. Other publications concern the more interesting possibility of directly controlling the contact pressure distribution as well as the size of the associated area of contact^{30,31} using truss and continuum finite elements, respectively. To our best knowledge, there is currently no previous literature available that covers transient frictional impacts and topology optimization. One notable recent paper is the one by Shobeiri³² in which many sources of nonlinearity, including contact, are taken into account during a transient topology optimization, but this paper does not include any form of friction.

In the present work we discretize a solid structure by the finite element method³³, apply time varying loads, resolve the structural displacements, velocities and accelerations for a period of time including frictional contact events, and obtain designs that minimize the maximum strain energy attained over space and time. The designs are obtained by gradient-based optimization methods, specifically density-based topology optimization, which is not topologically restricted by the initial design but requires an effective and efficient sensitivity analysis. The subsequent section 2 presents the physical model and the numerical methods used to solve the transient state problem with frictional contact. Section 3 covers the details of the proposed design parameterization and section 4 presents the topology optimization formulation, including the sensitivity analysis. Section 5 contains two numerical test examples which are solved to demonstrate the pros and cons of the proposed design methodology and finally section 6 concludes this work.

2 | GOVERNING EQUATIONS

2.1 | Dynamics

This section presents the mathematical model for transient structural problems with contact and friction. The presented model assumes plane strain and either small or large displacements, depending on the design example. To obtain the dynamic response of a structure discretized by the finite element method, the following discrete dynamic equation is solved

$$\mathbf{M}\ddot{\mathbf{u}} + \mathbf{D}\dot{\mathbf{u}} + \mathbf{F}_{int}(\mathbf{u}) = \mathbf{f}_t + \mathbf{f}_g + \mathbf{f}_c, \quad (1)$$

where \mathbf{u} is the structure's discretized deformation vector and dotted quantities refers to time derivatives such that $\dot{\mathbf{u}}$ and $\ddot{\mathbf{u}}$ represent velocities and accelerations, respectively. External forces consist of a time varying external load in vector \mathbf{f}_t , gravitational forces in vector \mathbf{f}_g and contact forces in vector \mathbf{f}_c .

The internal forces \mathbf{F}_{int} can be linear with respect to the displacements \mathbf{u} , i.e. $\mathbf{F}_{int} = \mathbf{K}\mathbf{u}$ with the structure's time-invariant stiffness \mathbf{K} . This case assumes a linear relationship between Cauchy stresses $\boldsymbol{\sigma}$ and linear strains $\boldsymbol{\varepsilon}_L$

$$\boldsymbol{\sigma} = \mathbf{C}\boldsymbol{\varepsilon}_L \quad (2)$$

where \mathbf{C} is the constitutive, plane strain stiffness matrix, which depends on the structure's elasticity modulus E and Poisson ratio ν . In general, the internal forces correspond to a non-linear function $\mathbf{F}_{int}(\mathbf{u})$, with a stiffness matrix \mathbf{K} which depends on \mathbf{u} . This is the case when geometrical nonlinearities are included by using e.g. the Saint Venant-Kirchhoff constitutive law

$$\mathbf{S} = \mathbf{C}\boldsymbol{\varepsilon}_{NL} \quad (3)$$

with the second Piola-Kirchhoff stresses \mathbf{S} and the Green-Lagrange strains $\boldsymbol{\varepsilon}_{NL}$.

The matrix \mathbf{M} represents the consistent mass of the system and \mathbf{D} models the damping of the system. For simplicity, the damping is modeled as Rayleigh damping such that

$$\mathbf{D} = \alpha\mathbf{M} + \kappa\mathbf{K} \quad (4)$$

where the coefficients α and κ are damping parameters. Note that the presented methodology is not dependent on the specific type of damping model. One could e.g. use either pure mass or pure stiffness damping, although the numerical examples presented include both terms for the sake of a more general presentation. It should be noted, though, that the combined effect of the two damping coefficients must be taken into account when choosing the step size for the numerical time integration. Relatively high damping is used in the examples of the present work to ensure a valid solution with relatively large time steps. This limitation can be improved by employing a higher order time integration scheme instead of the first order backward Euler integrator, described in the next section. In general the applicability of the method for slightly damped systems remains to be verified.

2.2 | Time integration

To integrate the structural response in time the first order implicit backward Euler scheme is used. This scheme approximates velocities and accelerations at time step n as

$$\begin{aligned} \dot{\mathbf{u}}_n &= \frac{1}{\Delta t} (\mathbf{u}_n - \mathbf{u}_{n-1}) \\ \ddot{\mathbf{u}}_n &= \frac{1}{\Delta t^2} (\mathbf{u}_n - \mathbf{u}_{n-1} - \Delta t \dot{\mathbf{u}}_{n-1}) \end{aligned} \quad (5)$$

where Δt is the time step size. The choice of an implicit scheme increases the computational cost of the time integration, but it is necessary as treatment of contact problems with explicit schemes results in numerically stiff systems³⁴. Alternatively, using an explicit scheme would require very small time steps to keep the error bounded and is therefore not a viable option. We remark, that the time integration scheme of Eq. (5) is unconditionally stable. Other popular time integration schemes, such as the Newmark method³⁵, have been tested but proved less robust. Higher order integration schemes for problems with contact is a subject of ongoing research³⁴. However, it should be noted, that the proposed method is directly applicable to other implicit time integration schemes with just minor modifications.

Although the backward Euler approximation is a very simple and numerically robust option for contact problems, one should still be aware that first order schemes, especially for coarse time steps, introduce excessive numerical damping. To ensure that the numerical damping, due to the time integrator, remains small compared to the structural damping from Eq. (4), suitable time steps were determined from numerical experiments for different levels of the structural damping parameters α and κ . A hybrid

scheme, with first order time integration and smaller time steps applied only during the impact and higher order time integration applied otherwise, would be a very useful extension but is not pursued in the present work.

2.3 | The contact formulation

The contact model used in this work is a simplified form of the one presented in³⁶. To allow a state of contact between an elastic body and a rigid obstacle, a set of nodes are considered to be potential contact nodes, denoted by an index i . For a two-dimensional problem, the contact formulation used here provides two extra equations per potential contact node to resolve the subvector \mathbf{f}_c^i holding the two force components in vector \mathbf{f}_c for node i .

Contact is considered against the boundary of a rigid obstacle, defined as the zero-level of a general signed distance function $g(x, y)$ that satisfies $\|\nabla g(x, y)\| = 1$, and is referred to as the gap function. The normal vector \mathbf{n} , pointing away from the obstacle may be obtained by differentiating the gap function with respect to both spatial dimensions. Using the gap function, impenetrability can be expressed as

$$g(\mathbf{u}) \geq 0. \quad (6)$$

In addition to fulfillment of the impenetrability condition of Eq. (6), certain other conditions must hold for the components of the contact forces. The normal component must point towards the elastic body and upon frictional sliding the tangential component must fulfill Coulomb friction. It is shown in³⁶, how the impenetrability, friction and relevant complementarity conditions can be expressed as a single non-smooth equality condition

$$\mathbf{Z}(\mathbf{f}_c^i, g^i, \dot{\mathbf{u}}^i, \mathbf{n}) = \mathbf{0} \quad (7)$$

in which both the gap function g , the normal vector \mathbf{n} and the velocity vector $\dot{\mathbf{u}}^i$ are functions of the displacements \mathbf{u} . The non-smooth \mathbf{Z} -function is defined as

$$\mathbf{Z}(\mathbf{f}_c^i, g^i, \dot{\mathbf{u}}^i, \mathbf{n}) = \mathbf{f}_c^i + [\mathbf{f}_c^i \cdot \mathbf{n} + r g^i]_- \mathbf{n} - P_{B(n, \mu[\mathbf{f}_c^i \cdot \mathbf{n} + r g^i]_-)}(\mathbf{f}_c^i - r \dot{\mathbf{u}}^i) \quad (8)$$

where μ is Coulomb's coefficient of friction and r is an augmentation parameter that may be chosen freely as long as $r > 0$. A note on selecting r is included in section 2.3.1. The negative part operator $[\cdot]_-$ is defined as

$$[x]_- = \begin{cases} -x & \text{if } x \leq 0 \\ 0 & \text{if } x > 0 \end{cases} \quad (9)$$

and $P_{B(n, \tau)}(\mathbf{d})$ is a projection of \mathbf{d} onto the plane with the normal vector \mathbf{n} and a circle of radius τ . The projection is defined as

$$P_{B(n, \tau)}(\mathbf{d}) = \begin{cases} \mathbf{T}_n \mathbf{d} & \text{if } \|\mathbf{T}_n \mathbf{d}\| \leq \tau \\ \tau \frac{\mathbf{T}_n \mathbf{d}}{\|\mathbf{T}_n \mathbf{d}\|} & \text{otherwise} \end{cases} \quad (10)$$

where $\|\cdot\|$ is the Euclidean norm and \mathbf{T}_n is the tangent plane projection defined as

$$\mathbf{T}_n = \mathbf{I} - \mathbf{n} \otimes \mathbf{n}. \quad (11)$$

where \otimes is the Kronecker product. The piecewise continuous partial derivatives of the \mathbf{Z} -function necessary for obtaining the consistent stiffness matrix can be found in³⁶.

2.3.1 | Selecting the augmentation parameter r

The only tunable parameter in the contact formulation, that the user needs to decide on beforehand is the augmentation parameter $r > 0$, and the result of the finite element analysis should, to a large extent, not depend on the choice. With topology optimization on top of the finite element analysis, the structure changes with each design, and thus the stiffness distribution changes with each design iteration. One option for selecting r would be to define it as a spatially varying field depending on the stiffness per location. This would correspond to larger r values in solid regions and smaller r values in void regions. However, numerical experiments have shown that it is more robust to work with a spatial constant r but tune its value during the finite element analysis. That is, if for one choice of r the solution of a timestep does not converge within a fixed number of Newton iterations, a new augmentation parameter r is sought in the range from 10^{-8} to 10^8 in 17 steps. In the unlikely case that Newton convergence is not achieved for any of the trial r values, the procedure is repeated with Newton steps scaled down by a factor of 0.95, corresponding to 5% Newton damping. This heuristic strategy has proven to be very robust for all considered examples of this manuscript.

2.4 | Solution of the global system

Expressing the governing equations outlined in the previous section in residual form one obtains the following system

$$\begin{aligned} \mathbf{R}_u &= \mathbf{f}_t + \mathbf{f}_g + \mathbf{f}_c - \mathbf{M}\ddot{\mathbf{u}} - \mathbf{D}\dot{\mathbf{u}} - \mathbf{F}_{\text{int}}(\mathbf{u}) = \mathbf{0} \\ \mathbf{R}_c^i &= -\frac{1}{r} \mathbf{Z}(\mathbf{f}_c^i, g^i, \dot{\mathbf{u}}^i, \mathbf{n}) = \mathbf{0} \quad i = 1, \dots, n_c. \end{aligned} \quad (12)$$

The nodal contact residual $\mathbf{R}_c^i \in \mathbb{R}^2$ contains the two components of the respective assembled residual vector $\mathbf{R}_c \in \mathbb{R}^{2n_c}$ corresponding to node i , with n_c denoting the number of potential contact nodes. This residual depends nonlinearly on both \mathbf{u} and \mathbf{f}_c . Both residual equations of Eq. (12) are solved in each time step to obtain the state variables \mathbf{u} and \mathbf{f}_c by application of Newton's method to the coupled system. It should be noted that the subsequent adjoint sensitivity analysis involves both state variables \mathbf{u} and \mathbf{f}_c as well as the corresponding residuals \mathbf{R}_u and \mathbf{R}_c . Note also that the Jacobian of the system in Eq. (12) is nonsymmetric even if friction is omitted. Although the global Jacobian is symmetrizable in the special case of frictionless contact, this is not essential for the method presented. The role of the scaling factor of $-1/r$ in the definition of \mathbf{R}_c is actually for ensuring a close to symmetric Jacobian, and thus, it is included only for numerical reasons.

3 | DESIGN PARAMETERIZATION

The framework presented in this work is based on the density method where each element is assigned a density value $0 \leq \rho \leq 1$ to indicate whether that element is considered to be solid ($\rho = 1$) or void ($\rho = 0$). A design may be identified as binary when all elements are either solid or void. Generally though, designs contain some fraction of so-called gray elements for which ρ is somewhere in between 0 and 1. Since intermediate densities are undesired, the robust formulation from³⁷ is employed, and this formulation is described in the following subsections. We remark that other approaches for reaching solid-void designs exist, e.g. by penalization as in³⁸ or the single realization projection filter as in³⁹, but that the robust formulation is chosen since this also provides a minimum feature size control, and renders designs insensitive to over- and under-etching.

3.1 | Filtering $\rho \rightarrow \tilde{\rho}$

As a first step a convolution type filtering process is applied on ρ in order to avoid the well-known problem of emerging checkerboard patterns and mesh dependence⁴⁰. In this work the density filter^{41,42}, defined in Eq. (13), is utilized for the filtering process. The filtered field element densities $\tilde{\rho}$ are constructed as a weighted average of neighbouring elements' densities.

$$\tilde{\rho} = \frac{\sum_{k \in \mathbb{N}} w_k \rho}{\sum_{k \in \mathbb{N}} w_k} \quad (13)$$

where \mathbb{N} is set of elements in the vicinity of an element with spartial center \mathbf{x}_0 , i.e.

$$\mathbb{N} = \left\{ k \mid \|\mathbf{x}_k - \mathbf{x}_0\|_2 \leq R_{\text{min}} \right\} \quad (14)$$

where R_{min} is the filter radius, \mathbf{x} denotes the spatial location of an element's center and the weighting factor w_k decays linearly with the distance between elements, according to

$$w_k = 1 - \frac{\|\mathbf{x}_k - \mathbf{x}_0\|_2}{R_{\text{min}}}. \quad (15)$$

Note that this version of the filter assumes elements of equal size.

3.2 | Projection $\tilde{\rho} \rightarrow \bar{\rho}$

The next step is to apply a series of projection filters on $\tilde{\rho}$, in order to obtain a series of eroded and dilated realizations of the base design while ensuring that these are close to being binary, i.e. strictly solid-void. The projection is done by the following smooth step function as presented in³⁷.

$$\bar{\rho} = \frac{\tanh(\zeta\eta) + \tanh(\zeta(\tilde{\rho} - \eta))}{\tanh(\zeta\eta) + \tanh(\zeta(1 - \eta))} \quad (16)$$

where ζ is the sharpness of the step function around the threshold value η . The design can be driven towards a solid-void state by gradually increasing ζ . Multiple realizations for different values of η can be considered. In this work, unless otherwise stated,

$$\eta \in \{0.3, 0.5, 0.7\} \quad (17)$$

which results in the three physical realisations $\bar{\rho}_d$, $\bar{\rho}_b$ and $\bar{\rho}_e$, representing a dilated, a blueprint and an eroded design respectively. In this work a ζ -continuation is enforced with ζ initiated at 1 and subsequently incremented in steps, either after 50 design iterations or if $\|\Delta\rho\| < 0.01$. The sequence of ζ values is reported along with each numerical example.

3.3 | Energy interpolation and large displacements

Geometric non-linearity is included in the second numerical example in order to account for the possibility of buckling of slender beams during optimization. To avoid instabilities in the void regions when using a geometrically nonlinear constitutive law, the elastic energy density in the solid and void regions are interpolated in such a way that linear elasticity is used in void, and nonlinear elasticity theory is used in solid. This energy interpolation, originally proposed by Wang et al and described in detail in⁴³, is characterized by the element wise interpolation parameter γ which depends on each element's physical design variable $\bar{\rho}$, and is evaluated as

$$\gamma(\bar{\rho}) = \frac{\tanh(\beta_1 \bar{\rho}_0) + \tanh(\beta_1(\bar{\rho} - \bar{\rho}_0))}{\tanh(\beta_1 \bar{\rho}_0) + \tanh(\beta_1(1 - \bar{\rho}_0))}. \quad (18)$$

The value of this function indicates whether an element is considered fully linear ($\gamma = 0$) or fully nonlinear ($\gamma = 1$), or somewhere in between. If nothing else is stated we employ $\beta_1 = 500$ and $\bar{\rho}_0 = 0.1$, following⁴³. The interpolation expression

$$\Pi = E [\Pi_0^{\text{NL}}(\gamma\mathbf{u}) - \Pi_0^{\text{L}}(\gamma\mathbf{u}) + \Pi_0^{\text{L}}(\mathbf{u})] \quad (19)$$

is then used for the interpolated stored elastic energy density Π . In this expression, Π_0^{NL} is the elastic energy density for the geometrically nonlinear constitutive law Eq. (3), for a reference material with $E = 1$. Similarly Π_0^{L} is the elastic energy density corresponding to the linear constitutive law Eq. (2), for the same reference material with $E = 1$.

This material interpolation, according to⁴³, leads to a nodal force vector \mathbf{F}_{int} for the discretized system in the form

$$\mathbf{F}_{\text{int}} = E \left(\gamma \mathbf{F}_{\text{int},0}^{\text{NL}}(\gamma\mathbf{u}) + (1 - \gamma^2) \mathbf{F}_{\text{int},0}^{\text{L}}(\mathbf{u}) \right), \quad (20)$$

where $\mathbf{F}_{\text{int},0}^{\text{NL}}$ and $\mathbf{F}_{\text{int},0}^{\text{L}}$ are respectively nodal force vectors for Saint Venant-Kirchoff and linearized elasticity with $E = 1$. Note that the dependencies of both E and γ on $\bar{\rho}$ need to be taken into account when evaluating the derivatives of \mathbf{F}_{int} with respect to $\bar{\rho}$ in the sensitivity analysis.

4 | TOPOLOGY OPTIMIZATION

Protecting occupants or payloads during impacts is an interesting design problem. First of all, it is necessary to define what exactly protection means. Typically, crashworthiness optimization deals with minimization of displacements or accelerations. It is e.g. common to minimize the acceleration of an occupant's head in a car crash. However, in other situations it might be desirable to avoid damage in a structural component, like e.g. the display glass of a falling smartphone. In such situations, some stress or strain based failure criterion is more appropriate. As an example, the elastic strain energy density, according to the following equation, is adopted in the present work as a metric of load and deformation intensity at a material point

$$W_h = \frac{1}{2} \boldsymbol{\varepsilon}^T \mathbf{C} \boldsymbol{\varepsilon} \quad (21)$$

with

$$\boldsymbol{\varepsilon} = \gamma \boldsymbol{\varepsilon}_{\text{NL}} + (1 - \gamma) \boldsymbol{\varepsilon}_{\text{L}} \quad (22)$$

that covers both cases of small and large displacements.

The strain energy W_h varies with location and time and its largest value indicates the most critical point for structural failure. In that sense, we aim at minimizing the maximum of W_h over time and space. Other strain based failure criteria or even a minimization of the maximum displacement or acceleration over a subdomain of interest could be implemented as objective function similar to what is proposed below for W_h .

For the rest of this work the total structural domain Ω is partitioned into smaller subdomains according to Fig. 1. A subdomain of prescribed solid is denoted as Ω_s , while the actual design domain is denoted as Ω_f . The objective value is evaluated in a subdomain Ω_h that can include parts of both the prescribed solid and design subdomains. The figure also indicates a subdomain Ω_c for evaluating a certain constraint function in part of Ω_f .

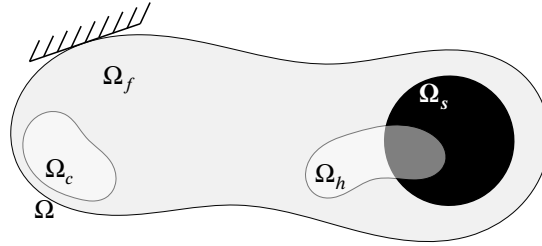


FIGURE 1 Partitioning of the domain Ω into smaller regions. Ω_f is the free region in which the optimizer can iteratively redistribute material to build a structure. Ω_s is a region of prescribed solid. Ω_h is the region in which the objective function is evaluated and Ω_c is a region where the constraint is evaluated.

Reminding that in this transient analysis, the strain energy density W_h is a function of both space and time, an approximation of the maximum W_h over space, is obtained first, by means of the p -norm of W_h at the center of all N_h elements in Ω_h

$$\phi_h(t) = \left(\sum_{e=1}^{N_h} W_h^{p_s} \right)^{\frac{1}{p_s}} \geq \max_s(W_h). \quad (23)$$

By this operation, one scalar value is obtained for every time instant, denoted here as $\phi_h(t)$. The p -norm formulation of Eq. (23) $\phi_h(t)$ overestimates the actual spatial maximum strain energy density at every time step, converging to the real value from above as p_s is increased⁴⁴.

The second step is to evaluate the p -mean of $\phi_h(t)$ over time. Using the trapezoidal integration rule, a single scalar value is obtained

$$\Phi_h = \left(\sum_{n=1}^{N_T} \frac{\phi_h(t_{n-1})^{p_t} + \phi_h(t_n)^{p_t}}{2} \Delta t_n \right)^{\frac{1}{p_t}} \leq \max_t(\phi_h(t)) \quad (24)$$

which approximates the maximum of W_h over space and time. The quantity Φ_h is hence used as the objective function. In Eq. (24), the total number of time steps is denoted as N_T . The p -mean formulation of Eq. (24) underestimates the actual temporal maximum strain energy density, converging to the real value as p_t increases, from below⁴⁴. We remark that this version of the p -mean does not contain the usual scaling with $1/N_T$, which instead is obtained through the multiplication by Δt_n .

This definition of the objective function includes two parameters that are to be chosen manually, i.e. the exponents $p_s \geq 1$ in Eq. (23) and $p_t \geq 1$ in Eq. (24). At the theoretical limit of $p_s = p_t = \infty$ the true maximum would be identified. Note that the parameters p_s and p_t are chosen differently in each of the numerical examples.

The generic optimization problem used in this work can be formally stated as

$$\begin{aligned} \min_{\rho} : & \max(\Phi_h^{\mathcal{K}}), \quad \mathcal{K} \in \{d, b, e\} \\ \text{s.t.} : & \frac{\bar{\rho}_d^T \mathbf{V}}{V_d^* V_0} - 1 \leq 0 \\ & : \frac{\Phi_c}{c^* \Phi_{c_0}} - 1 \leq 0 \\ & : 0 \leq \rho \leq 1 \end{aligned} \quad (25)$$

With this formulation the goal is to minimize the maximum objective, evaluated from an analysis of the three design realizations $\bar{\rho}_d$, $\bar{\rho}_b$ and $\bar{\rho}_e$. As indicated already, the objective function Φ_h is evaluated in the region Ω_h and the optimization is subject to three constraints.

The first constraint is a material constraint that restricts the optimizer to use no more than V_d^* of the total volume V_0 . The vector \mathbf{V} is a vector of individual element volumes. The volume constraint is enforced on the dilated design only, and is updated every 20 iteration by redefining $V_d^* = \frac{\bar{\rho}_d^T \mathbf{V}}{\bar{\rho}_b^T \mathbf{V}} V^*$, such that the blueprint design eventually satisfies the intended volume requirement of V^* . Enforcing the constraint on the dilated design prevents the optimizer from utilizing non-physical benefits from the projection scheme as illustrated in⁴⁵. We remark that the volume constraint is only used in the first test example.

The second constraint, which is only used in the second numerical example, aims at controlling the overall level of deformation of the structure by setting a bound to the maximum strain in an appropriately chosen subdomain Ω_c . This could be necessary, in order to exclude overly compliant designs from the solution space, for example due to usability and ergonomics requirements. The constraint function Φ_c is defined in the same manner as Φ_h in Eq. (24), but based on a different strain energy function

$$W_c = \frac{1}{2} \boldsymbol{\varepsilon}^T \boldsymbol{\varepsilon} \quad (26)$$

instead of Eq. (21). The corresponding exponents used in the definition of Φ_c are simply denoted as q_i and q_s instead of p_i and p_s , respectively. With this definition, the constraint is enforced that Φ_c in the final design will be smaller or equal to c^* times the value Φ_{c_0} , obtained for a full solid design, where c^* is a user defined constant.

The third and final constraint are the usual bounds on the design variables. We remark that the physics are always satisfied as the physics are solved to a point of sufficient equilibrium, i.e the optimization problem is considered in the so-called nested formulation⁴⁶. The optimization is terminated based on whether one of the following conditions is reached: i) $\zeta = \zeta_{max}$ and $\|\Delta \bar{\rho}\| < 0.01$ or ii) a fixed upper limit of design iterations, I_{max} is reached. The fixed number of iterations is problem specific.

4.1 | Design sensitivities

The sensitivities of the objective function with respect to the design variables can be found efficiently by the adjoint method. In this work we employ the commonly used semi-discrete adjoint approach for time-dependent optimization problems^{47,48,49}. Following this methodology, the spatial part is considered in its discrete state and the sensitivity analysis is obtained using the "discretize then differentiate" approach. For the temporal part, however, the fully discrete approach results in a rather complex formulation which involves adjoint variables not only with respect to the mechanical equilibrium equation but also with respect to the temporal derivative approximations⁵⁰. For this reason, the "differentiate then discretize" approach is used for the temporal part, despite its small inconsistency which is especially pronounced for large time steps. The inconsistency, arising from the fact that the sensitivity analysis does not include the error introduced in the time discretization of the forward problem, diminishes with increasing number of time steps.

The process of obtaining design sensitivities for transient problems with the "differentiate then discretize" approach is outlined in⁴⁷ and⁴⁸. This method is extended in the present work, to the case of the mixed problem of Eq. (12), which does not only involve displacements but also contact forces as variables. The adjoint analysis must accordingly involve two types of multipliers, λ_u and λ_c , which are discrete over space, one for each of the two equations contained in Eq. (12). The objective function Φ_c is therefore augmented with two terms which are equal to zero under equilibrium

$$\bar{\Phi}_h = \Phi_h + \int_0^T \lambda_u^T \mathbf{R}_u + \lambda_c^T \mathbf{R}_c dt \quad (27)$$

and differentiation with respect to $\bar{\rho}$ leads to

$$d_{\bar{\rho}} \bar{\Phi}_h = d_{\bar{\rho}} \Phi_h + \int_0^T \lambda_u^T d_{\bar{\rho}} \mathbf{R}_u + \lambda_c^T d_{\bar{\rho}} \mathbf{R}_c dt. \quad (28)$$

By expressing the total derivatives in Eq. (28) in terms of partial derivatives, applying integration by parts with respect to time, noting that $\partial_{\bar{\rho}} \mathbf{R}_c = 0$, and rearranging terms, the derivative $d_{\bar{\rho}} \bar{\Phi}_h$, equivalent to $d_{\bar{\rho}} \Phi_h$, can be evaluated as

$$d_{\bar{\rho}} \bar{\Phi}_h = \partial_{\bar{\rho}} \Phi_h + \int_0^T \lambda_u^T \partial_{\bar{\rho}} \mathbf{R}_u dt \quad (29)$$

where, for Φ_h not depending on velocities or accelerations, λ_u is determined based on the backward problem

$$-\mathbf{M}^T \dot{\lambda}_u + \mathbf{D}^T \lambda_u - \mathbf{K}^T \lambda_u + \partial_u \mathbf{R}_c^T \lambda_c = -\partial_u \Phi_h \quad (30a)$$

$$\lambda_u + \partial_{f_c} \mathbf{R}_c^T \lambda_c = \mathbf{0} \quad (30b)$$

$$\lambda_u(T) = \lambda_c(T) = \dot{\lambda}_u(T) = \dot{\lambda}_c(T) = \mathbf{0}. \quad (30c)$$

Although only λ_u is required in Eq. (29), the system of Eqs. (30a) and (30b) has to be discretized and solved for both λ_u and λ_c , with the terminal values of Eq. (30c). We remark that, after discretization in time, this system is linear in λ_u and λ_c . In the present work, the same time integration scheme is used for the backward problem as for the forward problem, according to Eq. (5), for simplicity. However, there is, no expectation that using the same time integration for the forward and backward problem will account for the forward time discretization error in the sensitivity analysis. The only way to guarantee this would be by applying the more complex but more consistent "discretize then differentiate" approach^{50,51}.

The derivatives $\partial_u \mathbf{R}_c$ and $\partial_f \mathbf{R}_c$, appearing in Eqs. (30a) and (30b), correspond, respectively, to the lower left and lower right block matrices of the forward problem Jacobian and are therefore available at any time step. Other partial derivatives required for the sensitivity analysis are $\partial_{\bar{\rho}} \Phi_h$, $\partial_{\bar{\rho}} \mathbf{R}_u$, and $\partial_u \Phi_h$, with further details for their computation given in the Appendix A. Once $d_{\bar{\rho}} \Phi_h$ is known, application of the chain rule with regard to filter- and projection operations between ρ and $\bar{\rho}$, leads to the gradient $d_{\rho} \Phi_h$, used in the optimization according to³⁷. The same methodology is applied to obtain the derivative of the field constraint $d_{\rho} \bar{\Phi}_c$, where $\bar{\Phi}_c$ is an augmented version of Φ_c , defined as in Eq. (27).

5 | RESULTS

In this section, two different numerical examples are presented to demonstrate structural optimization of transient frictional impact problems. The first design problem can be considered to be an academic test problem and is based on linear-elastic frictional contact. The second example deals with protecting a payload during an impact from a fall in a field of gravity and includes geometric non-linearity.

As is always the case for optimization of non-convex problems, there is no guarantee to find a global minimum. Instead, a local minimum is the best one can achieve. Therefore one should ideally initiate the optimization process from various initial designs. All numerical examples have been implemented in MATLAB and the optimization routine used throughout this work is the Method of Moving Asymptotes by Svanberg⁵².

Specific problem parameters are listed in Table 1. Please note that although these parameters do not directly reflect specific real physical systems, the amount of Rayleigh damping employed ensure significant transient effects. Highly dynamic undamped systems are excluded from the numerical experiments of the present work as they would require prohibitively small time steps.

It should also be noted, the RAMP stiffness interpolation is used for both of the following examples with $p = 5$, $E_0/E_1 = 10^{-9}$ and $m_0/m_1 = 10^{-3}$. This choice of parameters ensures the suppression of spurious modes in the void region. For details, please confer Appendix B.

5.1 | Cantilever impact

The first numerical design problem is depicted in Fig. 2. Through one full cycle of loading the structure is, in the first half of the cycle, pulled upwards and away from the obstacle and in the second half of the cycle, the structure is pressed towards the obstacle. For this problem $p_s = p_t = 1$, such that the quantity minimized is the integral of the strain energy density for all time steps and all elements. The purpose of this example is to investigate the effect of including friction between the structure and the obstacle. For this problem, geometric non-linearities are neglected for the sake of simplicity. Moreover, there is no constraint for the strain energy, i.e the second constraint in Eq. (25) is omitted. We only resolve the finite element analysis, compute the objective and evaluate design gradients for the eroded design, since for the choice of $p_s = p_t = 1$ this design will always be the worst performing and therefore the realization that drives the optimization.

The design shown in Fig. 3a is obtained from an optimization without friction between the structure and the obstacle, starting from a uniform distribution of material fulfilling the volume constraint. To exploit the available support the optimizer builds a column between the applied load and the obstacle. The column is also supported with a bar that prevents it from bending.

The framework allows to take friction into account and obtain designs optimized for settings with friction. However, when starting from a uniform feasible design the optimizer often converge to a local minimum and thereby preventing a better performance, than simply omitting friction in the first place. Instead, to demonstrate the possibilities of the framework, we restart the optimization procedure with the result of the frictionless optimization, include friction and $\zeta = \zeta_{max}$. Following this procedure for 900 iterations with a friction coefficient of $\mu = 0.30$ yields the design shown in Fig. 3b.

Even though the two designs have the same topology there are still visible differences between the two. Most notably the anchoring of the column support has moved upwards. A crosscheck verifies the optimization results. In the presence of friction,

the design obtained without friction performs better with a new objective of $3.01 < 3.23$. However the design obtained explicitly with friction performs significantly better with an objective of $2.71 < 3.01$. If this design is used in a frictionless setting, a deterioration is observed, i.e. $3.48 > 3.23$.

It is also clear from both rows in table 2, that by introducing friction the objective decreases in general. This is expected as friction can be thought of as means of dissipating energy, ultimately causing a lower objective value.

Fig. 4 demonstrates 4 snapshots of the two transient finite element analyses for (the eroded versions of) the structures in Fig. 3a and 3b. The obstacle is drawn in some of the figures, and a detail view highlights the behavior near contact point. In these plots it is clear that the optimizer builds a structure that utilizes the friction at the interface. It is also clear how the optimizer achieves this by letting the tip of the column bend in such a way that it slides along the obstacle on its end-surface and not just the corner.

To further see the effect of applying friction, we demonstrate the trajectory of the lower right point of the domain for the eroded designs (i.e the physics the optimization is based upon). It is immediately evident that the friction has the expected consequences with respect to the physics i.e the sliding of the tip is restricted by including friction.

Name	Description	Unit	Numerical example	
			1	2
t	Structural thickness	m	1	
p	Stiffness penalization (RAMP)	-	5	
E_1	Young's modulus of solid	N/m ²	$1 \cdot 10^5$	
m_1	Mass density of solid	kg/m ³	$5 \cdot 10^{-3}$	
E_0/E_1	Stiffness contrast	-	10^{-9}	
m_0/m_1	Mass density contrast	-	10^{-3}	
ν	Poisson's ratio	-	0.3	
L	Problem length	m	18	0.035
R_{\min}	Density filter radius	m	0.35	0.0027
F_0	Amplitude of external forces	N	50	-
ω	Frequency of external forces	1/rad	20π	-
g	Gravitational acceleration	m/s ²	0	-9.82
μ	Coefficient of friction	-	{0.00, 0.30}	0.05
v_0	Prescribed initial velocity	m/s	0	-5
α	Rayleigh damping parameter	1/s	0.01	$1 \cdot 10^{-5}$
κ	Rayleigh damping parameter	s	0.001	$1 \cdot 10^{-6}$
V^*	Volume constraint value	-	0.3	-
c^*	Strain energy constraint	-	-	varies
p_s	Objective spatial exponent	-	1	5
p_t	Objective time exponent	-	1	5
q_s	Constraint spatial exponent	-	-	1
q_t	Constraint time exponent	-	-	1
T	Final time of simulation	s	0.1	0.0025
Δt	Constant time step size	s	$1.25 \cdot 10^{-4}$	-
Δt_0	Coarse time step size	s	-	$25 \cdot 10^{-5}$
Δt_1	Fine time step size	s	-	$6.25 \cdot 10^{-5}$
I_{\max}	Fixed upper limit of design iterations	-	900	300
r	Augmentation parameter	-	varies	varies
ζ	Projection steepness values	-	{1, 2, 3, ..., 16}	{1, 2, 4, 5, 6, 8}

TABLE 1 Parameters used in the numerical examples.

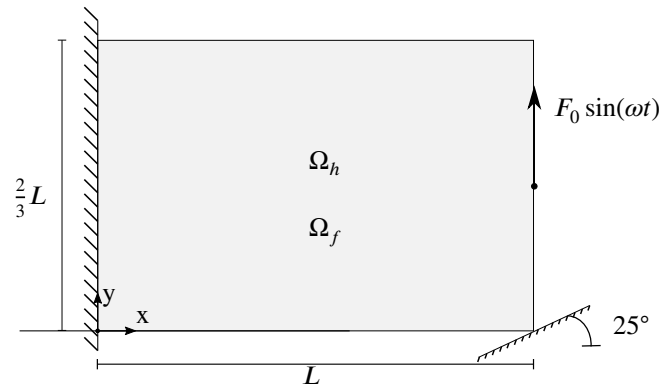
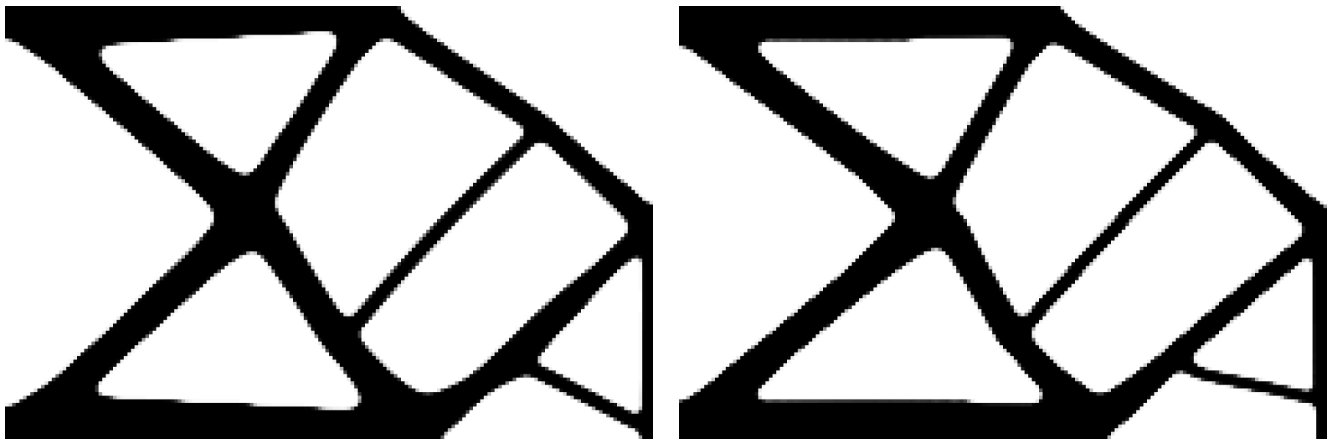


FIGURE 2 Cantilever impact. A linear-elastic (i.e. small displacements) domain is subjected to one cycle of a harmonic load as indicated. There is no initial gap between the undeformed structure and the obstacle. In this example, the integral of strain energy density, over Ω_h and all time steps, is minimized.



(a) Blueprint design for $\mu = 0.00$ starting from a feasible uniform material distribution.

(b) Blueprint design for $\mu = 0.30$ starting from the result of the frictionless optimization.

FIGURE 3 Two results to the problem laid out in Fig. 2

Optimized for	Evaluated for	
μ	0.00	0.30
0.00	3.23	3.01
0.30	3.48	2.71

TABLE 2 Crosscheck for the eroded versions of the designs in Fig. 3a and 3b.

5.2 | Drop test

The second design problem demonstrates how to protect a payload by minimizing the maximum strain energy density that arises during an impact. The frame is positioned at $y = 10^{-4}$ m above the rigid obstacle with an initial downward velocity of $v_0 = -5$ m/s. Minimizing the maximum strain energy density in a region Ω_h of the domain can be very useful as this can be related to a failure of the payload in this region. The schematic layout of the problem is shown in Fig. 6a.

In this problem one must have a sufficiently long time series, such that if all material in Ω_f is removed, Ω_h still collides with the obstacle. Furthermore for stiff structures, the impact will occur within a very narrow time frame making the problem numerically very stiff. As mentioned earlier, an implicit time stepping scheme is used to preserve stability of the time integration,

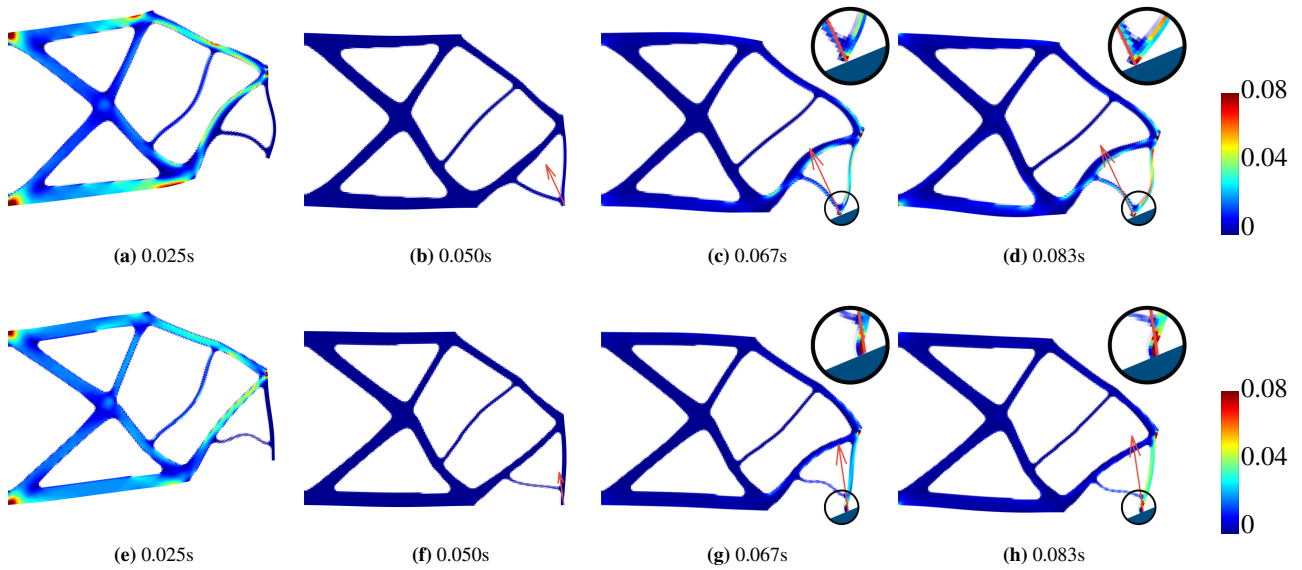


FIGURE 4 Snapshots of the two finite element analyses for the structures from Fig. 3a (with $\mu = 0.00$) and Fig. 3b (with $\mu = 0.30$).

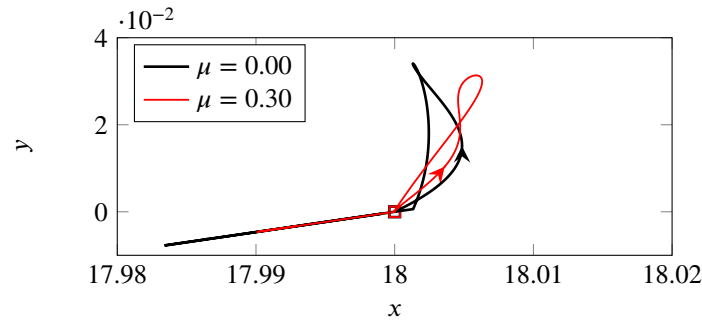


FIGURE 5 Trajectory of the lower right corner of the domain (i.e the tip of the column) for the eroded versions of the designs shown in Fig. 3a and 3b. The initial position is indicated with a square (\square) for both trajectories.

but if one wants to resolve the impact with more than one time step, and integrate for a fixed amount of time to ensure Ω_h reaches the obstacle, the simulation becomes computationally expensive. This becomes a severe limitation if one also wants to have a fine spatial discretization of the structure. Therefore, in order to decrease the computational cost of the time integration, an adaptive time stepping scheme is utilized to allow for a fine time discretization (Δt_1) during the impact, and a coarse time discretization (Δt_0) when the structure is not in contact. The fine discretization is also used for the subsequent 100 time steps after impact to capture the higher frequency transient response. Not resolving the impact with a sufficient number of time steps leads to abnormally high energy dissipation during the impact, and hence an adaptive time stepping is indispensable. Each of the two designs shown in Figure 3 completed after roughly 220 hours.

To obtain any form of physically sound designs it has proven necessary to include geometrical nonlinearity in the solid regions in order to account for buckling. Otherwise the optimizer exploits the suppressed possibility of buckling and provides non-physical ways to absorb the energy of the impact. Furthermore, in order to avoid excessively compliant designs, a limit is set to the overall compliance of the design by allowing the average strain measure Φ_c (i.e. $q_s = q_t = 1$) in the design domain (i.e. $\Omega_c = \Omega_f$) to grow only up to $c^* = 1000$ times the corresponding value $\Phi_{c_0} = 8.55 \cdot 10^{-8}$, obtained for a fully solid design. Solving the optimization problem with this constraint leads to the design shown in Fig. 6b.

The first thing to notice about the design in Fig. 6b, is that the internal block is not supported from below. It makes sense to prevent a direct transfer of forces from the obstacle to Ω_h . Instead, the optimizer has connected the payload to the outer frame

mainly by building a structure on the side of the payload and a small suspension from above. The reinforcement of the lower corners provides some extra stiffening in these regions. This helps to extend the impact time, as the structural parts above the reinforcements are thin and flexible - a property that helps to decelerate the internal block.

In Fig. 7, a time lapse of the displacement field and \log_{10} of the strain energy density in the payload is shown for a fully solid design, a reference design and the optimized design from Fig. 6b. The reference design is intended to exemplify an intuitive solution for the problem at hand. The actual maximum strain energy density in the payload region for the full solid design is $\max_{s,t}(W_h) = 0.0691$, whereas for the reference design it is equal to $\max_{s,t}(W_h) = 0.245$. That is, the reference design performs worse in this case compared to a full solid design. Comparing the response of the full solid design in 7a through 7e to the response of the reference design in Fig. 7f through 7j, it is clear how stress concentrations at the lateral connections in the reference design cause very localized strain energy density to occur in these regions, whereas the full solid design experiences a large strain energy density in larger parts of the domain. Fig. 7k through 7o illustrate the performance of the optimized structure. Here, it is clear how the optimizer prevents the payload from impacting, by a non-intuitive configuration of lateral connections that in effect prevent large stress concentrations. During the impact, the optimized structure experiences a true maximum strain energy density of $\max_{s,t}(W_h) = 0.007$. Compared to the reference design, the optimized design reduces the true maximum strain energy density within the payload to 3% of the reference value.

Fig. 8 shows how the spatial maximum approximation, $\phi_h(t)$, behaves for all three designs in Fig. 7, compared to the true maximum illustrated in red. As mentioned in the presentation of the p -norm formulations the spatial p -norm overestimates the real maximum, which can be seen in both plots.

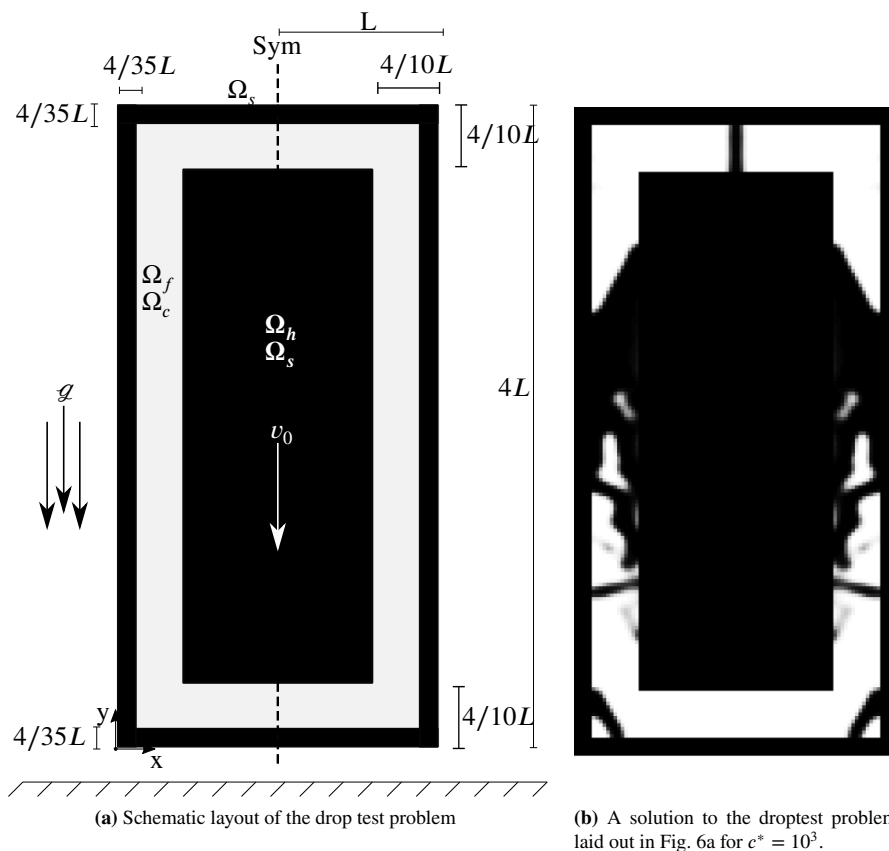


FIGURE 6 Drop test. A payload domain Ω_h is encapsulated by a solid outer frame and a design domain Ω_f . No boundary conditions keep the structure in place, as it falls with an initial velocity v_0 in a gravity field with gravitational acceleration $g = -9.82\text{m/s}^2$. The goal is to protect the payload by designing a structure in Ω_f which minimizes the maximum strain energy density in Ω_h during an impact with the rigid obstacle.

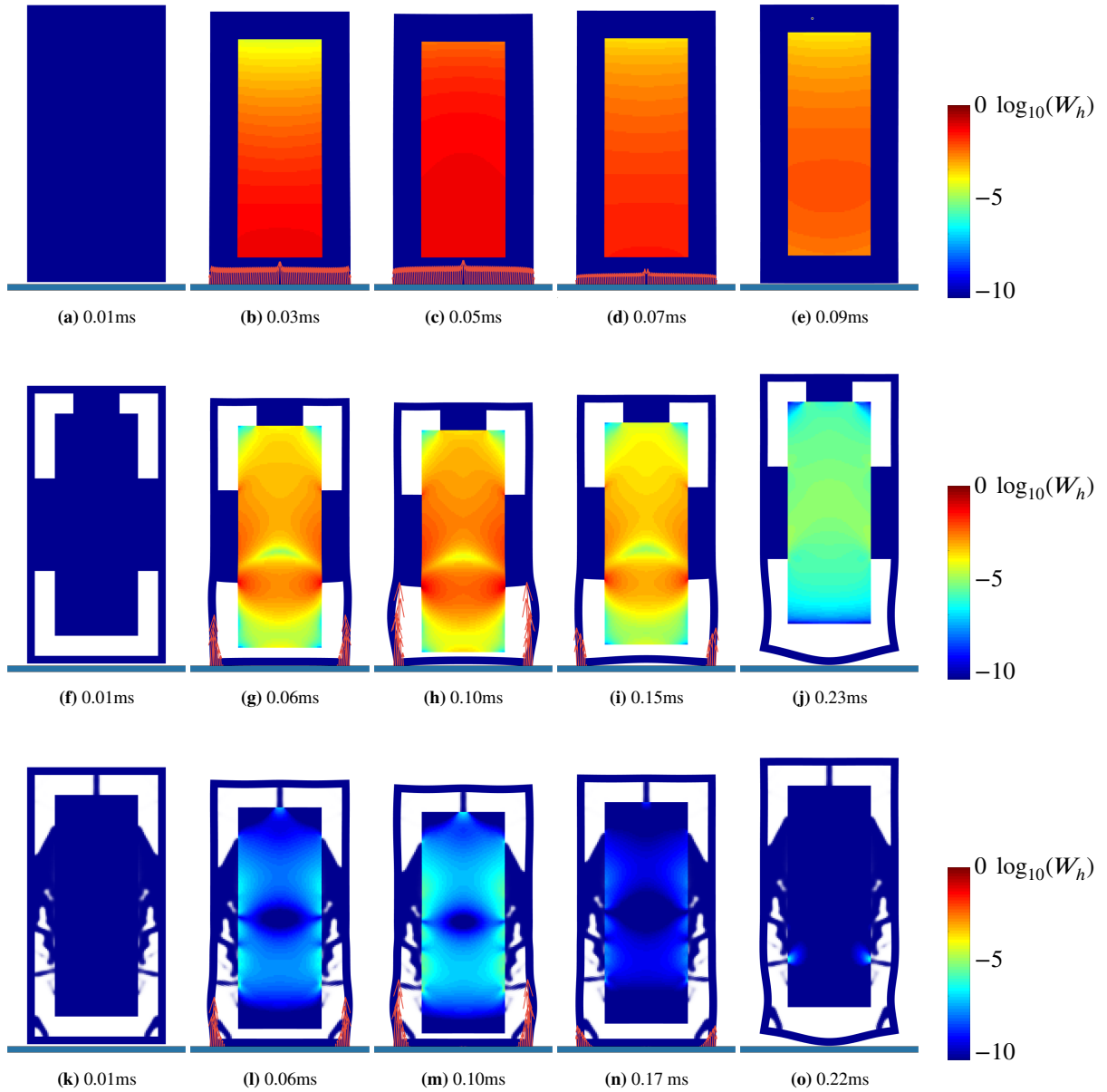


FIGURE 7 Time lapse of the displacement field and $\log_{10}(W_h)$ in Ω_h for a full solid design (a-e), a reference design (f-j) and the optimized design of Fig. 6b(k-o), at 5 different time steps. The full solid design has an objective value of $\Phi_h = 0.0324$, the reference structure has an objective value of $\Phi_h = 0.0326$, and the optimized structure has an objective value of $\Phi_h = 0.0014$. Displacements are magnified 30 times. Fig. (c), (h) and (m) are the time steps where the maximum strain energy density occurs.

The history of the objective function during optimization is shown in Fig. 9 together with a series of post evaluations using different values for p_s and p_t , as well as the real maximum value. Clearly, the objective function underestimates the real maximum value for all instances throughout the time series. This is, of course, expected as the temporal p -mean used here is known to underestimate the true maximum as mentioned earlier. It is interesting and worth noting that the offset caused by the double p -norm for the various choices of p_s and p_t remains rather constant relative to each realization. This makes it possible to conclude that the relatively low values used to produce the optimized results are sufficiently large to capture the behavior of the real maximum function.

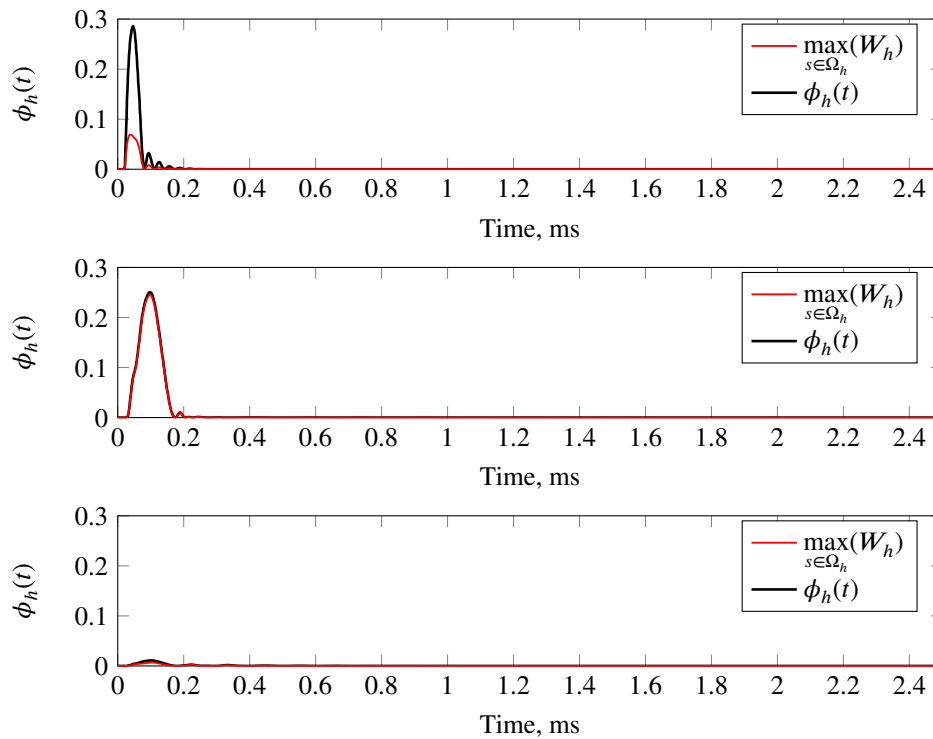


FIGURE 8 Time history of $\phi_h(t)$ for the full solid-, reference- and the optimized structure with $c^* = 10^3$.

To further investigate the evolution of the design from Fig. 6b, four snapshots of the design evolution are presented in Fig. 10. This figure demonstrates how the point of maximum strain energy density changes position in the domain as the optimization progresses. The red dot indicates the location of the true maximum strain energy density, and the size of the dot indicates the relative magnitude of the strain energy density across the four snapshots. The coloring of the four designs are based on the time step in which the true maximum strain energy density occurs, and the color scale is different between the figures, otherwise spatial variations of W_h would not be visible for some of the figures.

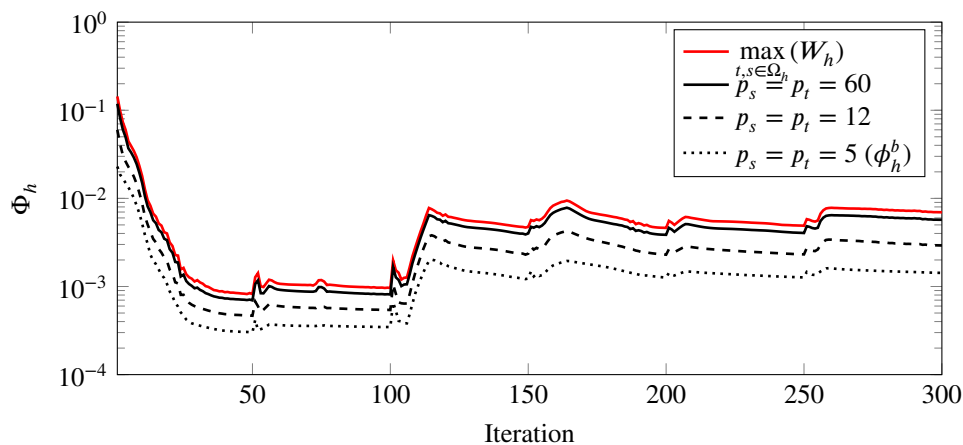


FIGURE 9 Evolution of objective values during optimization compared to true maximum strain energy density for various choices of p_s and p_t . The dotted line of $p_s = p_t = 5$ is the actual optimization settings.

By comparison of Fig. 9 and Fig. 10, it is possible to interpret the size of the red dot as the evolution of the objective function. That is, Φ_h is very large for the initial design. After 50 iterations Φ_h reaches its minimum as seen both in Fig. 9 and indicated by the small red dot in Fig. 10b. The small objective value is attributed to a large amount of intermediate density material at this iteration. The fact that intermediate densities improves the objective function further motivates the use of the robust design approach. By ζ -continuation, the measure of non-discreteness⁵³ within Ω_f is decreased from 45%, for the design in Fig. 10b, to 3.5%, for the design in Fig. 10d, at the cost of an increase in objective from $\Phi_h = 3.03 \cdot 10^{-4}$ to $\Phi_h = 14.27 \cdot 10^{-4}$.

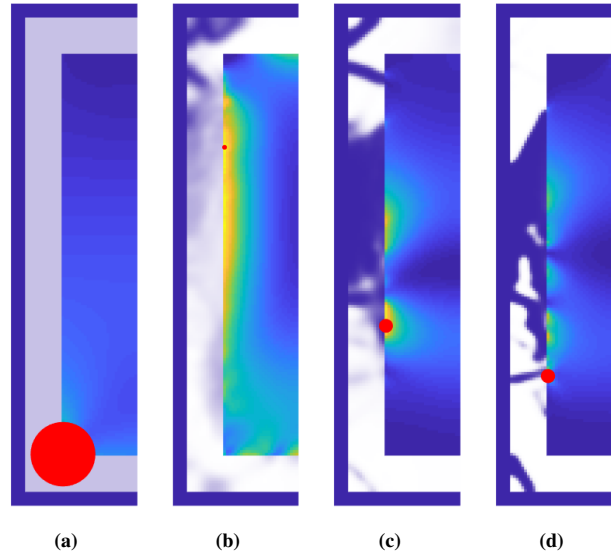


FIGURE 10 Path of the point of maximum strain energy density for the design shown in Fig. 6b. (a) design iteration 1, (b) design iteration 50 (lowest point of ϕ_h), (c) design iteration 175, (d) design iteration 300.

So far, the discussion has concerned only one result of the drop test example, namely the result with an overall compliance requirement corresponding to $c^* = 10^3$. Altering the required c^* leads, as expected, to different material layouts and Fig. 11 presents five different designs for five different choices of c^* . These results verify that increasing c^* allows the optimizer to construct designs with lower objective values. For lower choices of c^* , the optimizer constructs leg-like structures underneath Ω_h to prevent excessive strains in Ω_c but as the overall compliance constraint is relaxed, the support moves to the sides of Ω_h .

Using the current problem settings, each of the designs a-e presented in Fig. 11 took in the order of 100 wall-clock hours to produce. We remark that the computationally expensive procedure due to the combination of a large number of time steps and degrees of freedom is only mitigated by parallel execution of the transient finite element and sensitivity analysis for each of the three physical realizations, which is trivial. Further optimizations and parallelization are nevertheless required in order to make this approach applicable to larger, real world, engineering problems. The designs f-j in Fig. 11 are obtained by a post-process optimization in which the optimizer has to reduce the used amount of material by 20% compared to what it ended up using during the primary optimization. The post-process optimization is terminated once the design is feasible, requiring only between 12 and 15 iterations. By straightforward comparisons, it can be seen how the volume constraining post-process entails no guarantee for the optimizer to remove unwanted intermediate densities, as these are still beneficial for the structural performance. For structures: a and b, some of the gray features underneath the payload was removed, but only for one design c did the measure of non-discreteness decrease following the post-processing.

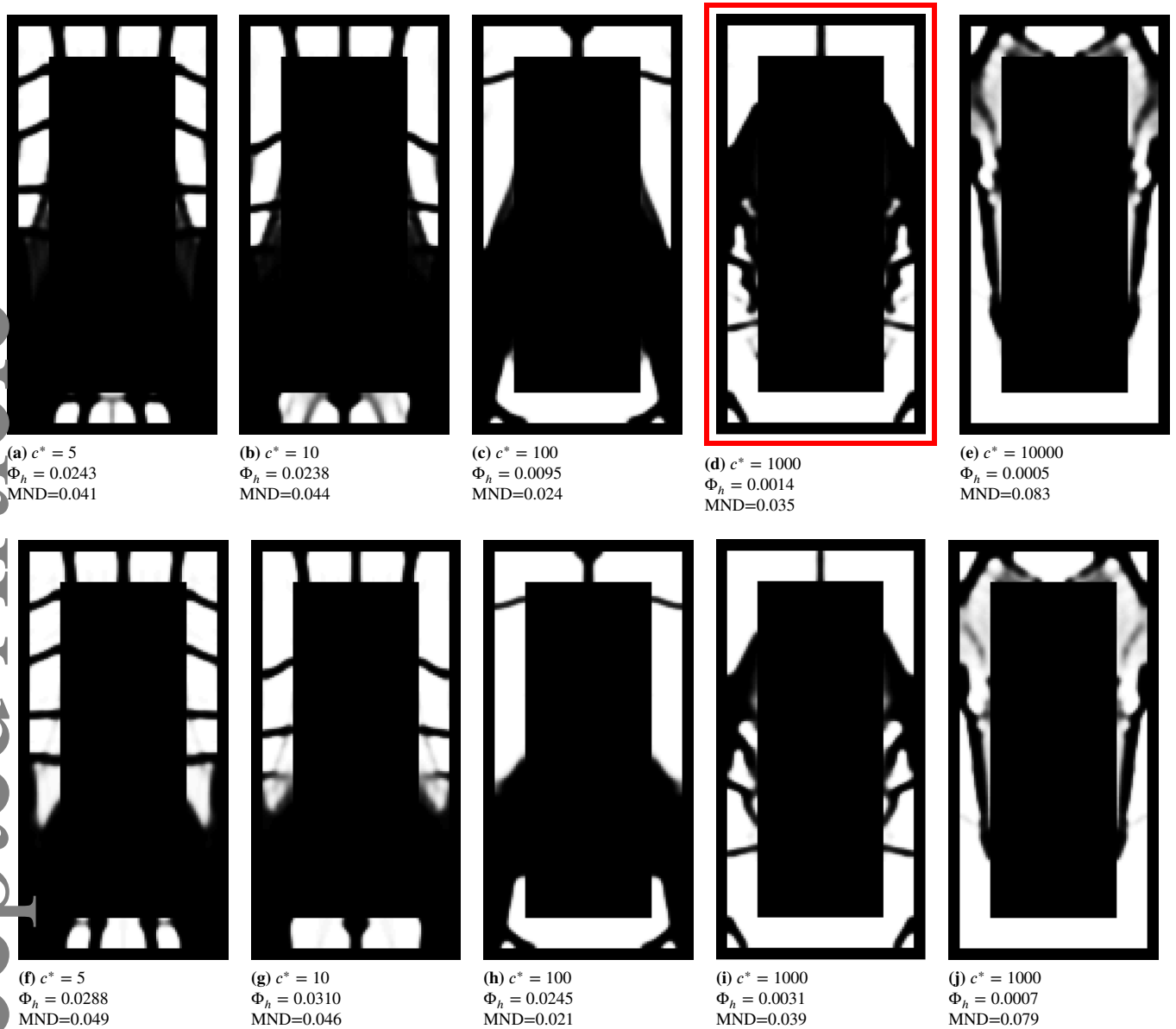


FIGURE 11 Payload protection with various constraint limits c^* for the strains in Ω_c . a-e: primary optimization, f-g: postprocess optimization to remove 20% material.

6 | CONCLUSIONS

A framework has been proposed that accounts for frictional impacts in density based topology optimization in the time domain and its capabilities have been demonstrated on two numerical examples.

The first example is a small displacements cantilever design problem which leads to rather intuitive designs which exploit both contact and friction for reducing a measure of dynamic compliance. The problem was run under frictionless conditions, as well as with Coulomb friction with $\mu = 0.30$, and a crosscheck performed between the two structures/settings, has demonstrated that the possibility of friction is indeed exploited. Each design was obtained after roughly 220 hours of computation.

The second numerical example aimed at demonstrating how to protect a falling payload from failure by designing a surrounding frame that minimizes the maximum strain energy density within the payload during an impact. Despite the numerical challenges and the high computational cost of roughly 100 hours per design, this example has shown the potential of the method

for producing close to black/white and physically sound designs, based on modeling of large displacements. In that relation, it should be noted that all runs were stopped at a steepness parameter of $\zeta = 8$, which means that some intermediate densities are expected to be present in the optimized designs.

Both numerical examples were solved with mass and stiffness damping included. The employed mass damping was insignificant but the employed stiffness damping was actually rather high. This choice was made in order to provide a valid solution, obtained with relatively large time steps, which is not dominated by the numerical damping of the first order backward Euler integrator. Implementing a higher order time integrator is challenging due to the presence of contact, but possible³⁴. This future step will allow to efficiently solve slightly damped systems without requiring prohibitively small time steps, and it will allow to check the validity of the method for slightly damped systems as well.

Despite having successfully demonstrated the validity of the proposed design methodology, the current numerical scheme is not without limitations. That is, the main shortcoming of the presented work is the long computation time needed to reach convergence. Several possibilities exist that could help alleviate this problem including: parallelization of the entire code using MPI, application of reduced order methods, use of more efficient time stepping schemes and the usage of in-exact Newton-Krylov methods to name just a few. It would also be interesting to study how the drop test designs change if the structure is optimized for multiple impact angles, e.g a 45° inclined fall leading to one of the corners impacting first.

In total, the presented framework is in general a valuable stepping stone for even more practical applications, and has the potential to provide valuable insight for designing protection of payloads, such as smartphones and insulin pens, from failure due to impacts.

ACKNOWLEDGMENTS

This work was funded by the Villum Foundation, Denmark as a part of the InnoTop VILLUM investigator project, Denmark.

Conflict of interest

The authors have no competing interests.

A | GRADIENT TERMS

This appendix contains some additional terms needed to complete the sensitivity analysis. The term $\partial_{\bar{\rho}}\Phi_h$ is evaluated based on the expressions

$$\begin{aligned}\partial_{\bar{\rho}}\Phi_h &= \Phi_h^{1-p_t} \sum_{n=1}^{N_T} \frac{\phi_h(t_{n-1})^{p_t-p_s} \sum_{e=1}^{N_h} \left(W_h^{p_s-1} \partial_{\bar{\rho}} W_h \right)_{t_{n-1}} + \phi_h(t_n)^{p_t-p_s} \sum_{e=1}^{N_h} \left(W_h^{p_s-1} \partial_{\bar{\rho}} W_h \right)_{t_n}}{2} \Delta t_n \\ \partial_{\bar{\rho}} W_h &= \frac{1}{2} \boldsymbol{\varepsilon}^T \mathbf{d}_{\bar{\rho}} \mathbf{C} \boldsymbol{\varepsilon} \\ &= \frac{1}{2} \boldsymbol{\varepsilon}^T \mathbf{C}_0 \boldsymbol{\varepsilon} \mathbf{d}_{\bar{\rho}} E\end{aligned}\tag{31}$$

where \mathbf{C}_0 is a reference initial stiffness matrix for $E = 1$, which means that $\mathbf{C} = E\mathbf{C}_0$.

The computation of $\partial_{\bar{\rho}}\mathbf{R}_u$ is based on

$$\begin{aligned}\partial_{\bar{\rho}}\mathbf{R}_u &= \mathbf{d}_{\bar{\rho}} E \left(\gamma \mathbf{F}_{\text{int},0}^{\text{NL}}(\gamma u) + (1 - \gamma^2) \mathbf{F}_{\text{int},0}^{\text{L}}(u) \right) + E \left(\mathbf{F}_{\text{int},0}^{\text{NL}}(\gamma u) - 2\gamma \mathbf{F}_{\text{int},0}^{\text{L}}(u) \right) \mathbf{d}_{\bar{\rho}} \gamma \\ \mathbf{d}_{\bar{\rho}} \gamma &= \frac{\beta_1 \operatorname{sech}^2(\beta_1(\bar{\rho} - \bar{\rho}_0))}{\tanh(\beta_1 \bar{\rho}_0) + \tanh(\beta_1(1 - \bar{\rho}_0))}.\end{aligned}\tag{32}$$

The computation of the gradient $\partial_u \Phi_h$ is based on

$$\partial_u \Phi_h = \Phi_h^{1-p_t} \sum_{n=1}^{N_T} \frac{\phi_h(t_{n-1})^{p_t-p_s} \sum_{e=1}^{N_h} \left(W_h^{p_s-1} \partial_u W_h \right)_{t_{n-1}} + \phi_h(t_n)^{p_t-p_s} \sum_{e=1}^{N_h} \left(W_h^{p_s-1} \partial_u W_h \right)_{t_n}}{2} \Delta t_n \quad (33)$$

$$\partial_u W_h = \epsilon^T \mathbf{C} (\gamma d_u \epsilon_{NL} + (1-\gamma) d_u \epsilon_L)$$

noting that W_h is always evaluated at the center of each element e .

B | MATERIAL INTERPOLATIONS

For static stiffness optimization, binary designs are favored when the stiffness of gray elements is penalized by a convex interpolation while subjected to a constraint on the amount of available material. The two most commonly used interpolation schemes are the SIMP interpolation^{2,54,53} and the RAMP scheme⁵⁵, which have both proven capable of solving static design problems. However, this is not the case for many problems considering dynamics, and therefore the following section will demonstrate why RAMP is the better option for this type of problems. We remark that a similar study can be found in⁵⁶.

Both schemes interpolate the physical density $\bar{\rho}$ of an element to the stiffness of that element E , from being E_0 at void to E_1 at solid. The stiffness of intermediate material is penalized by the penalization parameter p . The (modified) SIMP interpolation and the RAMP interpolation are stated below and can be seen plotted in Fig. 12.

$$E_{\text{SIMP}} = E_0 + (E_1 - E_0) \bar{\rho}^p \quad (34a)$$

$$E_{\text{RAMP}} = E_0 + (E_1 - E_0) \bar{\rho} \frac{1}{1 + p(1 - \bar{\rho})} \quad (34b)$$

The mass density m is interpolated linearly from m_0 in void to m_1 in solid.

$$m = m_0 + (m_1 - m_0) \bar{\rho} \quad (35)$$

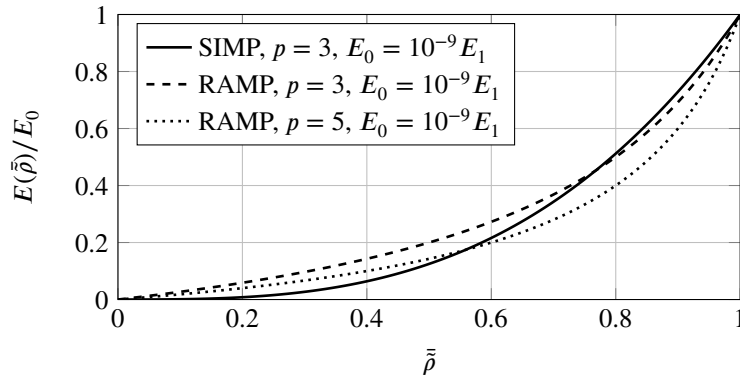


FIGURE 12 Comparison of (the modified) SIMP and the RAMP interpolation schemes. For the SIMP interpolation $p = 3$ is used⁵⁴. The RAMP interpolation is shown for both $p = 3$ and $p = 5$ for comparison to the SIMP curve.

Usually E_0 and m_0 are chosen to be several orders of magnitude smaller than E_1 and m_1 . For static problems a commonly used stiffness-contrast is $E_0/E_1 = 10^{-9}$ as this is a good approximation of the void stiffness properties. For transient problems, however, the choice of m_0/m_1 is also essential as it will greatly affect how the natural frequency of elements changes with $\bar{\rho}$. The natural frequency of an element is determined as

$$\omega(\bar{\rho}) = \sqrt{\frac{E(\bar{\rho})}{m(\bar{\rho})}}, \quad (36)$$

where $m(\bar{\rho})$ is according to Eq. (35). The choice of an interpolation scheme determines how ω varies with $\bar{\rho}$. Choosing the same scheme for both mass and stiffness, and the same contrast $E_0/E_1 = m_0/m_1$, will lead to $\omega = \sqrt{E_1/m_1}$, independent of $\bar{\rho}$. This is an unfortunate choice, because it will lead to the same natural frequency in void as in the solid. To prevent the optimizer from constructing and utilizing spurious void modes, one can require the natural frequency in void to be a fraction δ , e.g. $\delta = 10^{-3}$, of the natural frequency in solid, so that

$$\omega(0) = \delta \omega(1) \Rightarrow \sqrt{\frac{E_0}{m_0}} = \delta \sqrt{\frac{E_1}{m_1}} \Rightarrow \frac{m_0}{m_1} = \frac{1}{\delta^2} \frac{E_0}{E_1} \quad (37)$$

In Fig. 13 the evolution of $\omega(\bar{\rho})$ is shown for different magnitudes of δ using SIMP and RAMP for the stiffness interpolation respectively.

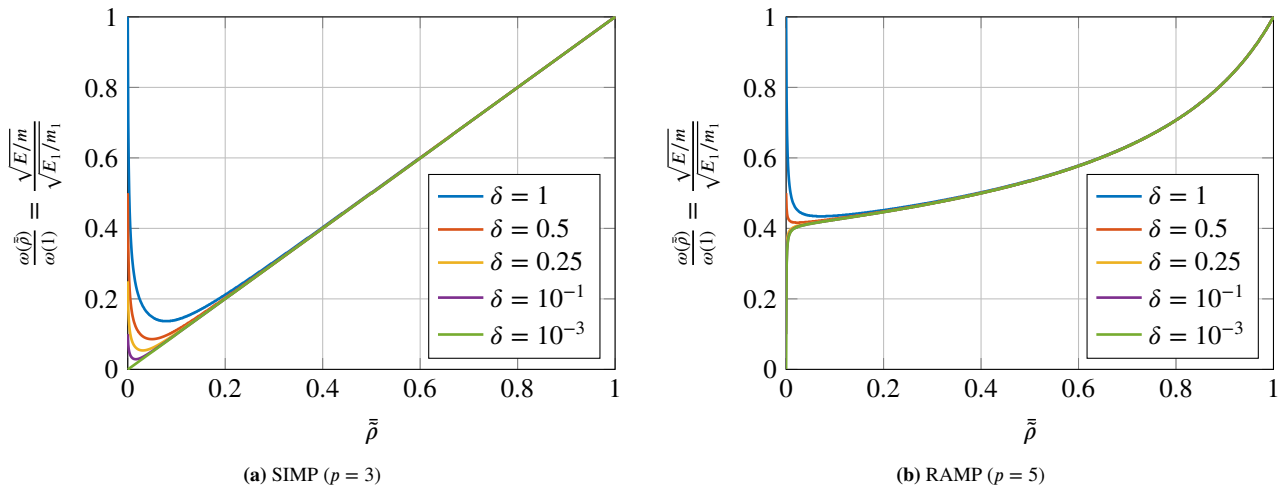


FIGURE 13 Relative natural frequency of an element of density $\bar{\rho}$ compared to a solid element, when $m_0/m_1 = 10^{-3}$ and the stiffness is interpolated using SIMP ($p = 3$) or RAMP ($p = 5$).

Considering Fig. 13a, one could choose $\delta = 10^{-3}$ to ensure that the natural frequency in void is three orders of magnitude smaller than the natural frequency of solid. However, Fig. 13a reveals an issue with the SIMP interpolation for transient problems: regardless of how small one chooses δ , the function $\omega(\bar{\rho})$ always exhibits its minimum at non-void, though this minimum moves closer to void as δ is decreased. For a small enough δ , one can completely alleviate this problem by using the RAMP interpolation, as seen in Fig. 13b. However, a good choice of δ also depends on the applied penalization parameter p .

In conclusion, with RAMP it is always possible to ensure a monotonically increasing natural frequency ω with increasing $\bar{\rho}$ by ensuring a non-negative gradient of Eq. (36) at $\bar{\rho} = 0$. This leads to the condition that for a fixed mass contrast, the stiffness E_0/E_1 should be chosen so that

$$\frac{E_0}{E_1} \leq \frac{m_0/m_1}{1 + (1 - m_0/m_1)p} \quad (38)$$

or, for a fixed stiffness contrast, the mass contrast m_0/m_1 should be chosen so that

$$\frac{m_0}{m_1} \geq \frac{(1+p)E_0/E_1}{1 + pE_0/E_1}. \quad (39)$$

Based on this study we therefore choose to work solely with the RAMP interpolation scheme for the remainder of the presented work with $m_0/m_1 = 10^{-3}$ and $E_0/E_1 = 10^{-9}$.

7 | DATA AVAILABILITY STATEMENT

The data that support the findings of this study are available from the corresponding author upon reasonable request.

References

1. Bendsøe MP, Kikuchi N. Generating optimal topologies in structural design using a homogenization method. *Computer methods in applied mechanics and engineering* 1988; 71(2): 197–224.
2. Bendsøe MP. Optimal shape design as a material distribution problem. *Structural optimization* 1989; 1(4): 193–202.
3. Bendsøe MP. *Topology optimization*. Springer . 2009.
4. Sigmund O. A 99 line topology optimization code written in Matlab. *Structural and multidisciplinary optimization* 2001; 21(2): 120–127.
5. Aage N, Andreassen E, Lazarov BS, Sigmund O. Giga-voxel computational morphogenesis for structural design. *Nature* 2017; 550(7674): 84.
6. Guedes J, Kikuchi N. Preprocessing and postprocessing for materials based on the homogenization method with adaptive finite element methods. *Computer methods in applied mechanics and engineering* 1990; 83(2): 143–198.
7. Groen JP, Sigmund O. Homogenization-based topology optimization for high-resolution manufacturable microstructures. *International Journal for Numerical Methods in Engineering* 2017.
8. Fronts propagating with curvature-dependent speed: Algorithms based on Hamilton-Jacobi formulations. *J. Comput. Phys.* 1988; 79(1): 12–49. doi: 10.1016/0021-9991(88)90002-2
9. Sethian JA. *Level set methods and fast marching methods: evolving interfaces in computational geometry, fluid mechanics, computer vision, and materials science*. 3. Cambridge university press . 1999.
10. Dijk vNP, Maute K, Langelaar M, Van Keulen F. Level-set methods for structural topology optimization: a review. *Structural and Multidisciplinary Optimization* 2013; 48(3): 437–472.
11. Andreasen CS, Elingaard MO, Aage N. Level set topology and shape optimization by density methods using cut elements with length scale control. *Structural and Multidisciplinary Optimization* 2020: 1–23.
12. Sigmund O, Maute K. Topology optimization approaches. *Structural and Multidisciplinary Optimization* 2013; 48(6): 1031–1055.
13. Haug EJ, Arora JS. Design sensitivity analysis of elastic mechanical systems. *Computer Methods in Applied Mechanics and Engineering* 1978; 15(1): 35–62.
14. Michaleris P, Tortorelli DA, Vidal CA. Tangent operators and design sensitivity formulations for transient non-linear coupled problems with applications to elastoplasticity. *International Journal for Numerical Methods in Engineering* 1994; 37(14): 2471–2499.
15. Chung YS, Cheon C, Hahn SY. Reconstruction of dielectric cylinders using FDTD and topology optimization technique. *IEEE Transactions on Magnetics* 2000; 36(4): 956–959.
16. Turteltaub S. Optimal material properties for transient problems. *Structural and Multidisciplinary Optimization* 2001; 22(2): 157–166.
17. Li Y, Saitou K, Kikuchi N. Topology optimization of thermally actuated compliant mechanisms considering time-transient effect. *Finite elements in analysis and design* 2004; 40(11): 1317–1331.
18. Wang H, Li G, Li E. Time-based metamodeling technique for vehicle crashworthiness optimization. *Computer Methods in Applied Mechanics and Engineering* 2010; 199(37-40): 2497–2509.
19. Pedersen CB. Crashworthiness design of transient frame structures using topology optimization. *Computer methods in applied mechanics and engineering* 2004; 193(6-8): 653–678.
20. Forsberg J, Nilsson L. Topology optimization in crashworthiness design. *Structural and Multidisciplinary Optimization* 2007; 33(1): 1–12.

21. Nakshatrala P, Tortorelli DA. Nonlinear structural design using multiscale topology optimization. Part II: Transient formulation. *Computer Methods in Applied Mechanics and Engineering* 2016; 304: 605–618.
22. Fang J, Sun G, Qiu N, Kim NH, Li Q. On design optimization for structural crashworthiness and its state of the art. *Structural and Multidisciplinary Optimization* 2017; 55(3): 1091–1119.
23. Petersson J, Patriksson M. Topology optimization of sheets in contact by a subgradient method. *International journal for numerical methods in engineering* 1997; 40(7): 1295–1321.
24. Patriksson M, Petersson J. A subgradient method for contact structural optimization. In: ; 1997: 295–314.
25. Zowe J, Kočvara M, Bendsøe MP. Free material optimization via mathematical programming. *Mathematical programming* 1997; 79(1-3): 445–466.
26. Kočvara M, Zibulevsky M, Zowe J. Mechanical design problems with unilateral contact. *ESAIM: Mathematical Modelling and Numerical Analysis* 1998; 32(3): 255–281.
27. Hilding D, Klarbring A, Petersson J. Optimization of structures in unilateral contact. *Applied Mechanics Reviews* 1999; 52(4): 139–160.
28. Lawry M, Maute K. Level set topology optimization of problems with sliding contact interfaces. *Structural and Multidisciplinary Optimization* 2015; 52(6): 1107–1119.
29. Niu C, Zhang W, Gao T. Topology optimization of elastic contact problems with friction using efficient adjoint sensitivity analysis with load increment reduction. *Computers & Structures* 2020; 238: 106296.
30. Klarbring A. On the problem of optimizing contact force distributions. *Journal of optimization theory and applications* 1992; 74(1): 131–150.
31. Kristiansen H, Poullos K, Aage N. Topology optimization for compliance and contact pressure distribution in structural problems with friction. *Computer Methods in Applied Mechanics and Engineering* 2020; 364: 112915.
32. Shobeiri V. Bidirectional evolutionary structural optimization for nonlinear structures under dynamic loads. *International Journal for Numerical Methods in Engineering* 2020; 121(5): 888–903.
33. Cook RD, others . *Concepts and applications of finite element analysis*. John Wiley & Sons . 2007.
34. Doyen D, Ern A, Piperno S. Time-integration schemes for the finite element dynamic signorini problem. *Siam Journal on Scientific Computing* 2011; 33(1): 223-249. doi: 10.1137/100791440
35. Newmark NM. A method of computation for structural dynamics. *Journal of the engineering mechanics division* 1959; 85(3): 67–94.
36. Poullos K, Renard Y. An unconstrained integral approximation of large sliding frictional contact between deformable solids. *Computers & Structures* 2015; 153: 75–90.
37. Wang F, Lazarov BS, Sigmund O. On projection methods, convergence and robust formulations in topology optimization. *Structural and Multidisciplinary Optimization* 2011; 43(6): 767–784.
38. Borrvall T, Petersson J. Topology optimization using regularized intermediate density control. *Computer Methods in Applied Mechanics and Engineering* 2001; 190(37-38): 4911–4928.
39. Guest JK, Prévost JH, Belytschko T. Achieving minimum length scale in topology optimization using nodal design variables and projection functions. *International journal for numerical methods in engineering* 2004; 61(2): 238–254.
40. Diaz A, Sigmund O. Checkerboard patterns in layout optimization. *Structural optimization* 1995; 10(1): 40–45.
41. Bourdin B. Filters in topology optimization. *International Journal for Numerical Methods in Engineering* 2001; 50(9): 2143–2158.

42. Bruns TE, Tortorelli DA. Topology optimization of non-linear elastic structures and compliant mechanisms. *Computer methods in applied mechanics and engineering* 2001; 190(26-27): 3443–3459.
43. Wang F, Lazarov BS, Sigmund O, Jensen JS. Interpolation scheme for fictitious domain techniques and topology optimization of finite strain elastic problems. *Computer Methods in Applied Mechanics and Engineering* 2014; 276: 453–472.
44. Duysinx P, Sigmund O. New Developments in Handling Optimal Stress Constraints in Optimal Material Distributions. *7th Symposium in Multidisciplinary Analysis and Optimization, AIAA/USAF/NASA/ISSMO* 1998: 1501-1509.
45. Sigmund O. Manufacturing tolerant topology optimization. *Acta Mechanica Sinica* 2009; 25(2): 227–239.
46. Bendsoe M, Sigmund O. Topology Optimization. Theory, Methods, and Applications. 1st. ; .
47. Dahl J, Jensen JS, Sigmund O. Topology optimization for transient wave propagation problems in one dimension. *Structural and Multidisciplinary Optimization* 2008; 36(6): 585–595.
48. Matzen R, Sigmund O, Jensen JS. *Topology Optimization for Transient Wave Propagation Problems*. PhD thesis. Technical University of Denmark (DTU), ; 2011.
49. Jensen JS, Nakshatrala PB, Tortorelli DA. On the consistency of adjoint sensitivity analysis for structural optimization of linear dynamic problems. *Structural and Multidisciplinary Optimization* 2014; 49(5): 831–837.
50. Pollini N, Lavan O, Amir O. Adjoint sensitivity analysis and optimization of hysteretic dynamic systems with nonlinear viscous dampers. *Structural and Multidisciplinary Optimization* 2018; 57(6): 2273–2289.
51. Lavan O. Adjoint sensitivity analysis and optimization of transient problems using the mixed Lagrangian formalism as a time integration scheme. *Struct. Multidiscip. Optim.* 2020; 61(2): 619–634. doi: 10.1007/s00158-019-02383-8
52. Svanberg K. The method of moving asymptotes—a new method for structural optimization. *International journal for numerical methods in engineering* 1987; 24(2): 359–373.
53. Sigmund O. Morphology-based black and white filters for topology optimization. *Structural and Multidisciplinary Optimization* 2007; 33(4-5): 401–424.
54. Bendsoe MP, Sigmund O. Material interpolation schemes in topology optimization. *Archive of applied mechanics* 1999; 69(9-10): 635–654.
55. Stolpe M, Svanberg K. An alternative interpolation scheme for minimum compliance topology optimization. *Structural and Multidisciplinary Optimization* 2001; 22(2): 116–124.
56. Jensen JS, Pedersen NL. On maximal eigenfrequency separation in two-material structures: the 1D and 2D scalar cases. *Journal of Sound and Vibration* 2006; 289(4-5): 967–986.

How to cite this article: , , , and (), , , .